Transport coefficients from first-principles calculations

T. J. Scheidemantel,[1] C. Ambrosch-Draxl,[2] T. Thonhauser,[1] J. V. Badding,[3,4] and J. O. Sofo[1,4,5]
[1]*Department of Physics, The Pennsylvania State University, University Park, Pennsylvania 16802, USA*
[2]*Institut für Theoretische Physik, Universität Graz, Universitätsplatz 5, A-8010 Graz, Austria*
[3]*Department of Chemistry, The Pennsylvania State University, University Park, Pennsylvania 16802, USA*
[4]*Materials Research Institute, The Pennsylvania State University, University Park, Pennsylvania 16802, USA*
[5]*Department of Materials Science and Engineering, The Pennsylvania State University, University Park, Pennsylvania 16802, USA*
(Received 10 April 2003; published 29 September 2003)

We present a method of modeling transport coefficients from first-principles calculations. We introduce the transport distribution that contains all electronic information and from which transport coefficients can easily be calculated. We use this method to analyze Bi_2Te_3 and calculate its transport coefficients for a comparison with experiment. The transport distribution gives an improved insight into the relationship between transport properties and electronic structure and is a valuable tool in the search for improved thermoelectric materials.

DOI: 10.1103/PhysRevB.68.125210 PACS number(s): 72.15.Jf, 72.10.Bg, 71.15.Mb

I. INTRODUCTION

The efficiency of a thermoelectric device depends on its geometry and on the product of the thermoelectric figure of merit (of the material in the device), Z,

$$Z=\frac{\sigma S^2}{\kappa}, \tag{1}$$

and temperature T. ZT is a function of the electrical conductivity σ, the thermoelectric power or Seebeck coefficient S, and the thermal conductivity κ. A modeling of these transport coefficients is valuable to the search for improved thermoelectric materials.

The usual strategy for modeling transport coefficients is semiempirical, utilizing a combination of a parametrized band structure and scattering mechanisms fitted to experimental results. Models to account for the effect of alloy scattering and scattering by acoustic and optical phonons and ionized and neutral impurities on the charge carriers are fitted to the experiment. Once this parametrization and fitting is accomplished, the model can be used to explore the effect of changes in composition, temperature, and doping level. This approach works reasonably well as long as the regions to be explored are not too far from the conditions of the experiment used to fit the model. Several examples of it can be found in the literature.[1–3] In view of these requirements, it is most applicable to the fine tuning of well established compounds. It is of very limited applicability for the exploration of thermoelectric materials, where the available experimental information is limited.

We introduce a different and complementary approach that attempts to obtain as much information as possible from first-principles calculations. The goal is to reduce the empirical information required to a minimum. First-principles total energy calculations within the local density approximation (LDA) using the linear augmented plane wave (LAPW) method are mature and can give detailed information about the electronic and structural properties of atoms, molecules, crystalline solids, surfaces, and interfaces.[4–6] The first step in our approach is to obtain the electronic structure from first-principles calculations, retaining the empirical modeling of the scattering mechanisms. However, many of the parameters needed to model the scattering events can be obtained from first-principles calculations. This approach is more general, and cannot compete in precision with the *ad hoc* models for a given material. It has the virtue, however, of offering valuable insight when little is known about a material. There is a trade-off between predictive power and precision.

II. THEORY

A. Definition of the transport coefficients

The perturbation of an electric field or temperature gradient induces electrical or thermal currents in a material.[7] The local relations between the electric field $\vec{E}$ and the temperature gradient ∇T with their corresponding electrical $\vec{J}$ and heat $\vec{J}_Q$ currents for an isotropic solid are

$$\vec{J}=\sigma\vec{E}-\aleph\nabla T,$$

$$\vec{J}_Q=T\aleph\vec{E}-\kappa_0\nabla T. \tag{2}$$

In the above equations we immediately recognize σ as the electrical conductivity. The Seebeck coefficient S, of paramount importance for thermoelectric applications, is defined as the voltage gradient produced in a sample by a given temperature gradient when the electrical current is zero. In accordance with this definition we can identify

$$S=\frac{\aleph}{\sigma}. \tag{3}$$

Finally, the electronic contribution to the thermal conductivity, κ_{el}, is defined as the heat current produced per unit of temperature gradient when the electrical current is zero,

$$\kappa_{el}=\kappa_0-T\sigma S^2. \tag{4}$$

The total thermal conductivity of the material will be the sum of this contribution and the corresponding lattice contribution. For a real material the currents need not be parallel to

the electric field or thermal gradient, and the transport coefficients are tensorial quantities.[8] This complicates the above relations slightly, but the essential definitions remain the same.

B. Calculation of the transport distribution and coefficients

To evaluate the transport coefficients defined in Sec. II A, we need a microscopic model of the transport process. We use the semiclassical approach given by the solution of Boltzmann's equation in the relaxation time approximation. For a comprehensive description of the method see the book by Nag.[9] Here we limit our description to a brief summary.

In general, the electrical current of carriers (electrons or holes) is defined as

$$\vec{J}=e\sum_{\vec{k}} f_{\vec{k}}\vec{v}_{\vec{k}}, \tag{5}$$

where e is the charge of the carriers. The sum runs over all quantum numbers of the system that, in the case of a crystalline solid, are the three components of the crystal momentum $\vec{k}$. $f_{\vec{k}}$ is the population of the quantum state labeled with $\vec{k}$, and $\vec{v}_{\vec{k}}$ is the group velocity associated with that state. The latter is defined as the gradient in reciprocal space of the dispersion relation (band structure) of the electrons in the crystal,

$$\vec{v}_{\vec{k}}=\frac{1}{\hbar}\frac{\partial\varepsilon_{\vec{k}}}{\partial\vec{k}}. \tag{6}$$

The population of the state $\vec{k}$ is the solution of Boltzmann's equation,

$$\frac{\partial f_{\vec{k}}}{\partial t}=-\vec{v}_{\vec{k}}\cdot\frac{\partial f_{\vec{k}}}{\partial\vec{r}}-\frac{e}{\hbar}\left(\vec{E}+\frac{1}{c}\vec{v}_{\vec{k}}\times\vec{H}\right)\cdot\frac{\partial f_{\vec{k}}}{\partial\vec{k}}+\left.\frac{df_{\vec{k}}}{dt}\right|_{scatt.}, \tag{7}$$

which states that the rate of change of the population is dependent on diffusion, the effect of electric ($\vec{E}$) or magnetic ($\vec{H}$) fields, or scattering. In the absence of fields, the stationary solution of Boltzmann's equation for fermions is the Fermi distribution function $f_0(\varepsilon_{\vec{k}})$. The population is the same for $\vec{k}$ and $-\vec{k}$, leading to a cancelation in the summation in Eq. (5), and zero net current flow.

Linearizing the above equation, using the relaxation time approximation for the scattering term, and in the absence of magnetic fields and temperature gradients, the population is

$$f_{\vec{k}}=f_0(\varepsilon_{\vec{k}})+e\left(-\frac{\partial f_0}{\partial\varepsilon}\right)\tau_{\vec{k}}\vec{v}_{\vec{k}}\cdot\vec{E}, \tag{8}$$

where τ is the relaxation time. The full space dependence of f is through the thermal gradient. Using this expression to calculate the current, the electrical conductivity tensor becomes

$$\boldsymbol{\sigma}=e^2\sum_{\vec{k}}\left(-\frac{\partial f_0}{\partial\varepsilon}\right)\vec{v}_{\vec{k}}\vec{v}_{\vec{k}}\tau_{\vec{k}}. \tag{9}$$

Similar expressions can be derived for the Seebeck coefficient and electronic thermal conductivity. For simplicity, however, we define the transport distribution (TD),[10]

$$\boldsymbol{\Xi}=\sum_{\vec{k}}\vec{v}_{\vec{k}}\vec{v}_{\vec{k}}\tau_{\vec{k}}. \tag{10}$$

The TD is the kernel of all transport coefficients. Once it is calculated, all transport coefficients necessary to determine ZT can be obtained directly. Using scalar coefficients,

$$\sigma=e^2\int d\varepsilon\left(-\frac{\partial f_0}{\partial\varepsilon}\right)\Xi(\varepsilon), \tag{11}$$

$$S=\frac{ek_B}{\sigma}\int d\varepsilon\left(-\frac{\partial f_0}{\partial\varepsilon}\right)\Xi(\varepsilon)\frac{\varepsilon-\mu}{k_BT}, \tag{12}$$

and for the thermal conductivity in Eq. (4),

$$\kappa_0=k_B^2T\int d\varepsilon\left(-\frac{\partial f_0}{\partial\varepsilon}\right)\Xi(\varepsilon)\left[\frac{\varepsilon-\mu}{k_BT}\right]^2, \tag{13}$$

where μ is the chemical potential and k_B is Boltzmann's constant. Equations (11)–(13) show that the TD contains all material dependent information pertinent to transport properties.

III. IMPLEMENTATION IN THE WIEN2k PACKAGE

To calculate the TD [Eq. (10)] the group velocity, the energy, and the relaxation time are needed for each $\vec{k}$–point. As mentioned in Sec. I, in this first implementation we take the group velocity from the first-principles calculations but estimate the relaxation times. A direct calculation of the group velocity, using the definition given in Eq. (6), is numerically difficult to implement. Electronic structure codes usually evaluate the band energies in a numerical mesh for the Brillouin zone sampling; therefore, the group velocity must be evaluated as a numerical derivative. This differentiation requires the use of a computationally costly, very fine grid. One method currently being implemented to reduce the computational cost employs a Fourier expansion of energy bands. The Fourier expansion can then be analytically differentiated to obtain the group velocity.[11] However, even if the computational cost can be reduced, real materials usually have several bands crossing the Fermi level and each other which poses a difficulty for this strategy.

Our approach is different. The group velocity is related to the momentum

$$\vec{v}_{n,\vec{k}}=\frac{1}{m}\vec{p}_{n,\vec{k}}=\frac{1}{m}\langle\psi_{n,\vec{k}}|\vec{\hat{p}}|\psi_{n,\vec{k}}\rangle \tag{14}$$

if the coefficients are evaluated at zero field. The band index n has been omitted up to this point in order to make the expressions simpler. To recover the full expressions it is sufficient to replace $\vec{k}$ by $(n,\vec{k})$ in all the indices. The last part of Eq. (14) is the intraband optical matrix element. These matrix elements are available in the optical properties package of the full-potential linearized augmented plane wave (FP-

LAPW) WIEN2k code.[12,13] We have implemented the calculation of transport coefficients described here as one of the modules of this package. Although, with this method, a dense mesh around the Fermi surface is needed to properly evaluate the transport coefficients, the requirement is not as high as with numerical differentiation, and the band crossing problem is naturally avoided. Having the optical matrix elements and the electronic band structure, all that remains in order to calculate the TD is the relaxation time.

In this first implementation of the transport code, we restrict the scattering mechanisms to those most relevant for compound semiconductors: scattering by acoustic phonons (deformation potential and piezoelectric), nonpolar optic phonons, ionized and neutral impurity atoms, and alloy scattering.[9] The parameters entering the expressions for the scattering, such as the deformation potential constant, piezoelectric constant, sound velocity, density, optical phonon frequency, and others, are presently taken from experiment. In the future we plan to evaluate some of them from first principles, but important open questions remain as to the best approaches.

All semiconductors used as thermoelectric materials are doped to optimize the figure of merit. First-principles calculations, however, are performed for stoichiometric compounds. To treat doping we have to resort to approximations. We have chosen to use the simplest approach, the rigid band approximation. We will assume that the band structure remains unchanged as we move the Fermi level up and down to simulate *n* and *p* doping, respectively. This approximation is good as long as the doping levels used are not high enough to change the bonding properties of the material. To test this approach, we have calculated the TD and transport coefficients for Bi_2Te_3. Sufficient experimental data has been obtained for Bi_2Te_3 to allow for a rigorous evaluation of the method.

IV. APPLICATION TO Bi_2Te_3

A. Computational details

The crystal structure of Bi_2Te_3 belongs to the spacegroup $R\bar{3}m$ with atoms stacked along the trigonal axis, Te(1)-Bi-Te(2)-Bi-Te(1). For all calculations we used the experimental rhombohedral cell parameters of $a=10.48$ Å and $24.16°$.[14] Density functional theory was employed as implemented in the WIEN2k code, utilizing the full potential APW+lo method.[13] The generalized gradient approximation as described by Perdew, Burke, and Ernzerhof was used for the exchange and correlation potential.[15] A muffin-tin radius, R_{mt}, of 1.48 Å separated the core from the interstitial region on both the Bi and Te atoms. An $R\cdot k_{max}$ value of 10, and a G_{max} value of 20, were used corresponding to 950 basis functions in the wave function expansion and 13 259 stars in the interstitial region respectively. The calculation was converged with $231\vec{k}$ points, while the optical matrix elements were calculated for a dense mesh of 11 050 $\vec{k}$ points in the irreducible wedge of the Brillouin zone. Because of the large spin-orbit (SO) effects in Bi_2Te_3, eigenstates were calculated up to 10.0 Ry and included in the SO calculation.[16,17] The sum over $\vec{k}$ points in Eq. (10) was evaluated with the Blöchl integration method.[18] A constant, anisotropic relaxation time (discussed in Sec. IV B 2), and experimentally determined lattice thermal conductivities of 1.5 W/mK along the basal plane and 0.7 W/mK along the trigonal axis were used at all doping levels.[19] $\partial f_0/\partial\varepsilon$ was evaluated at 300 K for all integrals.

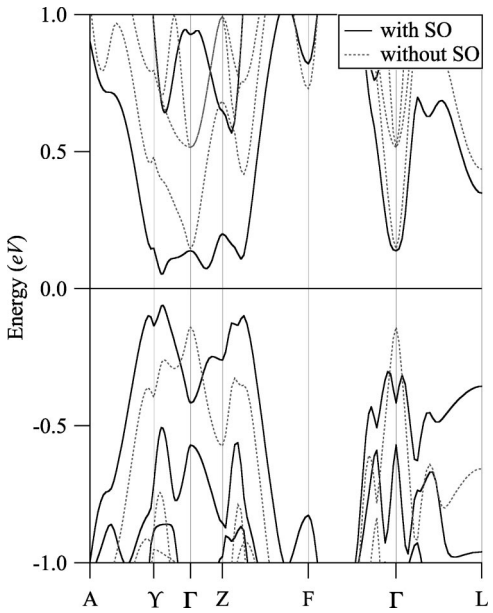

FIG. 1. The electronic structure of Bi_2Te_3 is shown with and without SO. The figure shows the importance of SO in Bi_2Te_3 by moving band edges away from Γ.

B. Results

1. Band structure

To calculate transport properties an accurate electronic structure is required. Our calculated band structure along commonly explored high symmetry lines is shown in Fig. 1. We have also included a point labeled Υ, chosen such that the line Υ-Γ passes through the lowest conduction band (LCB) and highest valence band (HVB) edges. We find the band edges in the mirror plane, yielding six LCB and six HVB pockets as a result of threefold rotational symmetry and inversion symmetry. This has been confirmed by experiment.[20,21] The calculated band gap, $E_g=0.11$ eV, is in good agreement with experiment.[22] Past reports found the LCB edge along the Γ-*Z* line using the linear muffin tin orbital (LMTO)-LDA and FP-LAPW (WIEN97) methods.[23,24] This yields only two carrier pockets due to inversion symmetry.

SO effects are very important in Bi_2Te_3 because its constituent elements are heavy. The second variational method used in our calculation depends on the number of states included in the SO perturbation term. This is controlled by the energy window of states included. When states up to 10.0 Ry are included, the LCB shows six pockets. In contrast, when the default window is used, -7.0–1.5 Ry, only two pockets are obtained. We studied the dependence of the energy dif-

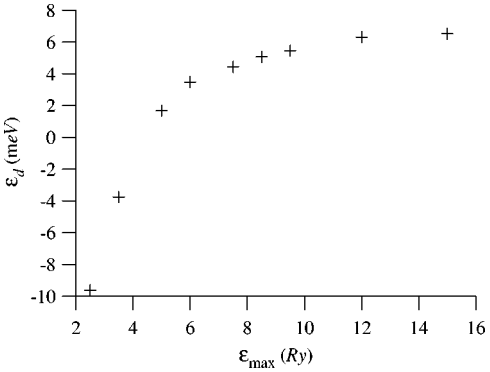

FIG. 2. The energy difference between the two states, $\varepsilon_{\Gamma Y}$ and $\varepsilon_{\Gamma Z}$, is shown vs the upper limit of the energy window used. An upper limit above 8.0 Ry is sufficient to produce reliable results.

ference between the LCB states along Γ-Z and Γ-Y on the upper energy limit of states included in the perturbation, and found that the two states' energies move with respect to each other as the upper limit of the energy window is varied. Figure 2 shows the energy difference between the LCB edge that we obtain and the state on the Γ-Z line, $\varepsilon_d = \varepsilon_{\Gamma Z} - \varepsilon_{\Gamma Y}$, as a function of the upper energy limit. The calculations converge with the Γ-Y pocket lower in energy, $\varepsilon_d > 0$, leading to six pockets in the LCB. An upper limit of 8.0 Ry seems to be sufficient. Reference 24 does not mention the energy window used. Other parameters such as R_{mt}, and the number of $\vec{k}$ points used, are also different, however these differences do not affect the results. We also compared results between LDA and generalized gradient approximation calculations and found no differences in the location of the band edges.

More recently, Youn, et al. found six pockets in both the HVB and LCB using another implementation of the FP-LAPW method and the local density approximation for the exchange and correlation potential.[25] Our LCB edge is the same as, but our HVB edge is slightly different than that found by Youn *et al.* We find the HVB edge at (0.652,0.579,0.579) and a nearby secondary edge 40 meV below, at (0.539,0.368,0.368), referred to as ***c*** and ***b***, respectively in Fig. 3(a) of Ref. 25. Youn *et al.* find the HVB edge at ***b***, and a secondary edge, 3.8 meV lower in energy, at ***c***. These differences are small and within the expected precision of our method.

With a well converged band structure, and electron velocities calculated as described in Sec. III, we were able to calculate the TD. The integrations were then carried out for different values of the chemical potential to simulate doping as discussed in Sec. III. We first compare our results for the Seebeck coefficient, the electrical conductivity, and *ZT* with experiment. We then present a general analysis of the TD, the power factor (PF), and *ZT*.

2. Comparison of calculated transport coefficients with experimental results

As is customarily done in thermoelectric literature, we plot S_{xx} (the Seebeck coefficient along the basal plane), on the *y* axis, and σ_{xx} on the *x* axis for samples with different doping concentrations. Figure 3 shows experimental data of doped Bi_2Te_3 documented in Ref. 26 along with our calculated values of the Seebeck coefficient. In calculating the Seebeck coefficient, the constant relaxation time cancels from both integrals [Eqs. (11) and (12)], eliminating it as a fitting parameter. We can, however, use τ to fit the Seebeck coefficient with its corresponding electrical conductivity. A constant relaxation time of $\tau_{xx} = 2.2 \times 10^{-14}$ s, which gives the best agreement in the intrinsic region, was used at all doping levels. We obtain a better correspondence on the *n*-doped side of the graph, but overall, the calculated data agree well with experiment considering that only the relaxation time was adjusted to fit the data.

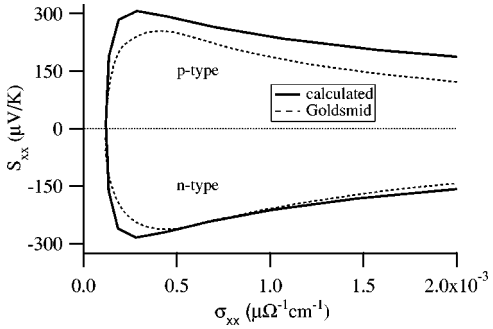

FIG. 3. Calculated Seebeck coefficients with experimental data from Ref. 26.

The anisotropy of Bi_2Te_3's electrical conductivity is well documented.[27] The conductivity along the basal plane can be more than four times greater than that along the trigonal axis (*zz* direction). This is enough to compensate for a lattice thermal conductivity along the trigonal axis that is half of that along the basal plane. Since the lattice thermal conductivity is comparable to the electronic contribution in the range of reasonable doping, Bi_2Te_3 is used as a thermoelectric device with conduction along the basal plane.[26] Figure 4 shows the anisotropy of our calculated electrical conductivity along with experimental data.[28] The data represented by the dotted line were calculated using the relaxation time determined above for conductivity in all directions. The agreement between experimental data and theory is very good. However, if we use an anisotropic relaxation time, $\tau_{xx} = 2.2$

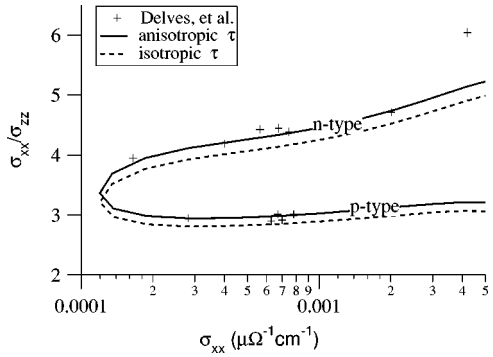

FIG. 4. Calculated electrical conductivity with experimental data from Ref. 28.

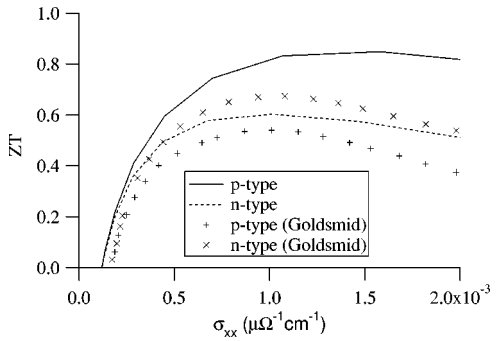

FIG. 5. Estimated values of *ZT* with data from Ref. 26.

$\times 10^{-14}$ and $\tau_{zz}=2.1\times 10^{-14}$ s, the solid line in Fig. 4 shows even better agreement with experiment. Since this relaxation time is only slightly anisotropic, less than a 5% difference between directions, Bi_2Te_3's strong anisotropy is a result of its electronic structure, i.e., if any arbitrary, isotropic, constant relaxation time were used, the strong anisotropy of the conductivities would still be apparent. This supports the validity of our calculated band structure. The strong disagreement starting near $\sigma=4\times 10^{-3}\ \Omega^{-1}\,\mathrm{cm}^{-1}$ ($n \sim 10^{20}\ \mathrm{cm}^{-3}$) could be attributed to the failure of the rigid band model at high doping concentrations.

Using the experimentally determined lattice thermal conductivity of intrinsic Bi_2Te_3, we were able to make an estimate of *ZT*. Figure 5 shows experimentally determined *ZT*'s along with our calculated values.[26] Both sets of data are for *ZT* calculated along the preferred direction. Again, agreement between calculated values and experiment is quite good. Confident that the band structure and velocities used in the calculations produced reliable results, we now analyze those results to determine which features of Bi_2Te_3's band structure give rise to a large PF and *ZT*.

3. Analysis of transport coefficients

Figure 6 shows several calculated properties plotted as a function of chemical potential (i.e., versus doping in the rigid band model): The TD, density of states (DOS), Seebeck coefficient, PF, and *ZT*. The doping levels represented over the entire range of the plots may be unattainable, but it allows a complete analysis of what gives rise to good electronic properties and *ZT*. For reference, carrier concentrations up to $10^{20}\ \mathrm{cm}^{-3}$ correspond to chemical potentials between -0.17 eV (p-doped) and 0.17 eV (n-doped). First we will focus on the PF and Seebeck coefficient because of the value of *ZT* is complicated by contributions from the lattice thermal conductivity.

In Fig. 6, there is no evident correlation between the structure of the TD or DOS and peaks in the PF. Looking at Eqs. (11)–(13), $\partial f_0/\partial\varepsilon$ dictates the range of the integral. Because 5 kT, the width of $\partial f_0/\partial\varepsilon$, is small compared to the bandwidth, we can approximate the TD as a line,

$$\Xi(\varepsilon)\approx a(\varepsilon-\mu)+b, \tag{15}$$

where a and b are, respectively, the slope and the height of the TD. Evaluating Eqs. (11) and (12) using this approximation, it is easy to show that the PF behaves as

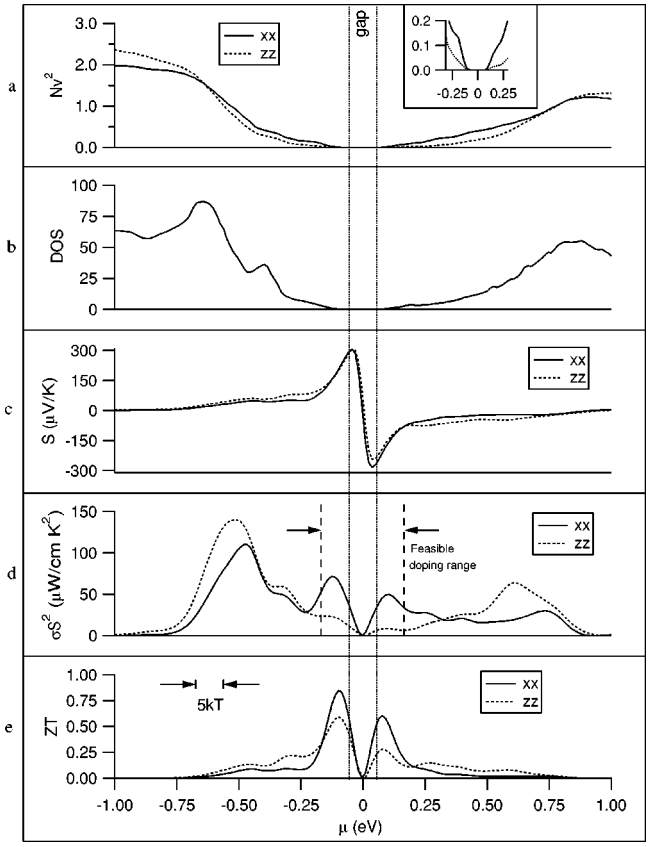

FIG. 6. The (a) TD, (b) density of states, (c) Seebeck coefficient, (d) PF, and (e) *ZT* are all plotted vs the chemical potential. Lines depicting the size of Bi_2Te_3's energy gap span the plot. Lines indicating a reasonable doping range ($n,p<10^{20}\ \mathrm{cm}^{-3}$) are shown with the PF (d).

$$\sigma S^2\propto\frac{a^2}{b}. \tag{16}$$

The PF grows with increasing slope, or decreasing height of the TD. This is evident near -0.6 eV in Fig. 6(a), where the two TDs intersect. Here, the *xx* and *zz* directions have equal values of TD, but along the *zz* direction the slope is larger. Equation (16) predicts a larger PF for the TD with the larger slope. Figure 6(d) shows that the PF along the *zz* direction is indeed greater than that along the *xx* direction. This behavior also manifests itself near 0.75 eV on the *n*-doped side of Fig. 6(a).

The Seebeck coefficient, plotted in Fig. 6(c) shows more structure in the range of attainable doping levels near the Fermi energy. The approximation of Eq. (15) gives a Seebeck coefficient that behaves as a/b. This makes it more sensitive to a larger height of the TD (or larger electrical conductivity). Comparing this to Eq. (16), and by looking at Fig. 6, we see that the optimum Seebeck coefficient does not correspond to the optimum PF.

All but two of the peaks in the PF lie outside the range of reasonable doping. The benefit of these peaks away from the gap is moot, due to a large κ_{el} that would accompany heavy doping. Figure 6(e) shows *ZT*'s calculated from our data and the experimentally determined lattice thermal conductivity

discussed in Sec. IV B 2. One *p*-type maximum and one *n*-type maximum, corresponding to 5×10^{19} and 4×10^{19} cm^{-3} carrier concentrations, respectively, remain at reasonable doping levels. Both agree with experimentally optimized *ZT*'s. The inset of Fig. 6(a) shows a closer view of the TD that gives rise to these peaks. This shows the importance of the band gap in Bi_2Te_3. Near the gap, *b* can be very small while *a* can be large. This does not imply, however, that the gap needs to be small or that this condition only occurs near the gap.

V. CONCLUSION

Starting from basic transport equations we have defined the TD, which is obtainable from first-principles calculations. The TD contains all the electronic information necessary to describe a material. The optical matrix elements needed are already available in the LAPW basis. The method was tested on a material that has been thoroughly investigated, Bi_2Te_3, and the calculated transport coefficients are in agreement with those reported by experiment. The TD was also used to analyze the relationship between the electronic structure of Bi_2Te_3 and its thermoelectric properties. The transport coefficients can be easily extracted from the slope and value of the transport distribution alone. The power factor is proportional to the square of the slope and inversely proportional its value.

The method presented here should prove valuable in the search for improved thermoelectric materials. Despite the known limitations of first principles calculations in the treatment of alloys and the limitations of the relaxation time approximation, the method gives a rapid and reliable way to efficiently screen potential candidates for thermoelectric materials. Furthermore, from this analysis, insight can be obtained into which features of a material make it exhibit high *ZT*, such as which bands contribute to the transport process and what crystal structural features are associated with the high *ZT*. This knowledge opens the way to tailoring the electronic bands to produce more efficient materials. We are presently incorporating a better description of the scattering mechanisms beyond the constant relaxation time approximation into the code, including the effect of scattering by acoustic and optical phonons, ionized impurities, disorder due to alloying, and intraband and interband transitions. This is the first step towards the ultimate goal of a parameter free evaluation of thermoelectric transport coefficients.

ACKNOWLEDGMENT

The authors would like to thank Prof. G. D. Mahan for valuable discussions which made this work possible. This research was funded by NFS Grant No. DMR-02-05125. Furthermore, it was supported in part by the Materials Simulation Center, a Pennsylvania State University MRSEC and MRI facility.

[1] D. L. Rode, *Transport Phenomena*, in *Semiconductors and Semimetals*, Vol. 10, edited by R. K. Willardson and A. C. Beer (Academic, New York, 1975).
[2] C. B. Vining, J. Appl. Phys. **69**, 331 (1991).
[3] J. O. Sofo, G. D. Mahan, and J. Baars, J. Appl. Phys. **76**, 2249 (1994).
[4] P. Hohenberg and W. Kohn, Phys. Rev. **136**, B864 (1964).
[5] W. Kohn and L. J. Sham, Phys. Rev. **140**, A1133 (1965).
[6] *Density Functional Theory*, Vol. 337 of *NATO Advanced Study Institute, Series B: Physics*, edited by E. K. U. Gross and R. M. Dreizler (Plenum, New York, 1995).
[7] H. B. Callen, *Thermodynamics* (Wiley, New York, 1960) Chap. 17.
[8] W. E. Bies, R. J. Radtke, H. Ehrenreich, and E. Runge, Phys. Rev. B **65**, 085208 (2002).
[9] B. R. Nag, *Electron Transport in Compound Semiconductors* (Springer Verlag, Berlin, 1980).
[10] G. D. Mahan and J. O. Sofo, Proc. Natl. Acad. Sci. U.S.A. **93**, 7436 (1996).
[11] G. K. H. Madsen (private communication).
[12] C. Ambrosch-Draxl and J. O. Sofo (unpublished).
[13] P. Blaha, K. Schwarz, G. K. H. Madsen, D. Kvasnicka, and J. Luitz, *WIEN2k, An Augmented Plane Wave+Local Orbitals Program for Calculating Crystal Properties* (Karlheinz Schwarz, Techn. Universität Wien, Austria, 2001). ISBN 3-9501031-1-2.
[14] S. Nakajima, J. Phys. Chem. Solids **24**, 479 (1963).
[15] J. P. Perdew, K. Burke, and M. Ernzerhof, Phys. Rev. Lett. **77**, 3865 (1996).
[16] D. Singh, *Planewaves, Pseudopotentials, and the LAPW Method* (Kluwer Academic, Boston, 1994).
[17] J. Kuneš, P. Novák, M. Diviš, and P. M. Oppeneer, Phys. Rev. B **63**, 205111 (2001).
[18] P. E. Blöchl, O. Jepsen, and O. K. Andersen, Phys. Rev. B **49**, 16 223 (1994).
[19] H. J. Goldsmid, Proc. Phys. Soc. London, Sect. B **69**, 203 (1956).
[20] R. B. Mallinson, J. A. Rayne, and R. W. Ure, Jr., Phys. Rev. **175**, 1049 (1968).
[21] V. V. Sologub, A. D. Goletskaya, and R. V. Parfen'ev, Fiz. Tverd. Tela (Leningrad) **14**, 914 (1972) [Sov. Phys. Solid State **14**, 783 (1972)].
[22] R. Sehr and L. R. Testardi, J. Phys. Chem. Solids **23**, 1219 (1962).
[23] S. K. Mishra, S. Satpathy, and O. Jepsen, J. Phys.: Condens. Matter **9**, 461 (1997).
[24] P. Larson, S. D. Mahanti, and M. G. Kanatzidis, Phys. Rev. B **61**, 8162 (2000).
[25] S. J. Youn and A. J. Freeman, Phys. Rev. B **63**, 085112 (2001).
[26] H. J. Goldsmid, *Thermoelectric Refrigeration* (Plenum, New York, 1964).
[27] J. Nagao, M. Ferhat, E. Hatta, and K. Mukasa, Phys. Status Solidi B **219**, 347 (2000).
[28] R. T. Delves, A. E. Bowley, D. W. Hazelden, and H. J. Goldsmid, Proc. Phys. Soc. London **78**, 838 (1961).